Significance of H2 and CO release during thermal treatment of natural phyllosilicate-rich rocks

Benoît Quesnel, Laurent Truche, Michel Cathelineau, Marie-Christine Boiron, Malgorzata Lempart-Drozd, Thomas Rigaudier, Arkadiusz Derkowski, Eric C. Gaucher

Significance of H_2 and CO release during thermal treatment of natural phyllosilicate-rich rocks

Benoît Quesnel[1]*, Laurent Truche[2], Michel Cathelineau[1], Marie-Christine Boiron[1], Malgorzata Lempart[3], Thomas Rigaudier[4], Arkadiusz Derkowski[3], Eric C. Gaucher[5]

[1] *Université de Lorraine, CNRS, CREGU, GeoRessources, F-54000 Nancy, France*

[2] *Université Grenoble Alpes, CNRS, ISTerre, F-38000 Grenoble, France*

[3] *Institute of Geological Sciences, Polish Academy of Sciences, Research Centre in Kraków, Senacka 1, 31-002 Kraków, Poland*

[4] *CRPG-CNRS, Université de Lorraine, UMR 7358, 54501 Vandoeuvre-lès-Nancy Cedex, France*

[5] *TOTAL, CSTJF, avenue Larribau F-64018 Pau – France*

* *Corresponding author: benoit.quesnel.1@ulaval.ca*

Keywords: natural hydrogen, hydrogen isotope, dehydrogenation, chlorite, talc

Highlights

- H_2 is produced by dehydrogenation of Fe-poor phyllosilicates
- H_2 produced by dehydrogenation has very low δD values
- Large mineral-H_2 hydrogen isotope fractionations are induced by dehydrogenation
- Dehydrogenation is a potential H_2 source term in the hydrogen geochemical cycle

Abstract

Phyllosilicates may trap hydrogen (H_2) in the crust, but they may also produce it through various processes, including oxidative dehydrogenation. The dehydrogenation temperature depends on the type and composition of the phyllosilicates considered, but it may be as low as 300 ˚C. Here, we document the release of H_2 and CO during thermal treatment of chloritite (300 ˚C) and talc (500 ˚C) from the Trimouns deposits (Eastern Pyrenees, France). Thermal release of gases coupled to stable isotope analysis has been used to recover and characterize H_2 and CO, the two detected gases. Hydrogen content may be as high as 7 ppm with δD_{H2} values ranging from -258 ‰ to – 224 ‰ for sub-pure chloritite and -140 ‰ for pure talc. CO content ranges between 3 ppm and 35.3 ppm with very homogeneous $\delta^{13}C_{CO}$ values between -27.6 ‰ and -25.7 ‰. This study supports the idea that H_2 was produced during

experiments by dehydrogenation. The origin of CO remains enigmatic, but its carbon isotope composition suggests a link to the few amounts of graphite documented in chloritite and talc from the deposit. This work also reports extensive hydrogen isotope fractionation between H_2 produced by dehydrogenation and both talc and chloritite. Dehydrogenation of phyllosilicates is a potential source term of H_2 in numerous magmatic-hydrothermal settings and must thus be accounted for in the budget of the H_2 geochemical cycle.

1. Introduction

Recent investigations have demonstrated that phyllosilicates are excellent traps for gaseous species migrating in the Earth's crust. Entrapment of CH_4 or CO_2 by phyllosilicates is already well documented in the context of shale gas exploration, CO_2 sequestration, and nuclear waste storage (Busch et al., 2016; Klewiah et al., 2020; Sanz et al., 1983; Ziemiański et al., 2020). High H_2 contents (up to 500 ppm) have been recently reported in clay-rich rock surrounding the Cigar Lake U-ore deposit in Canada (Truche et al., 2018). In this latter case, H_2 was released sequentially within minutes after thermal heating of the samples within the 80 – 300 ˚C temperature window.

For this study, the first intention was to study the paleo-gas(es) entrapped or adsorbed in talc and chloritite from the Trimouns deposit (France). In this area, hydrothermal fluids could have been enriched in H_2, CH_4, and CO as lherzolites are serpentinized in the talc deposit surroundings. This work proposes quantifying and measuring the stable isotope composition of gases released during the heating of natural chloritite and talc samples from the Trimouns deposit (Pyrenees, France) and discussing their origin and geological significance.

2. Material and Methods

2.1 Material

Chloritites and talc from the Trimouns deposit (Fig. 1) result from the hydrothermal alteration of host rocks (pegmatites, micaschists and dolostone) by primary brines circulation (Boiron et al., 2005; Boiron et al., 2007; Boulvais et al., 2006; Moine et al., 1989; Parseval (de) et al., 2004; Quesnel et al., 2019). In this study, three types of samples from the Trimouns deposit and La Porteille area - the north extension of the main deposit - have been studied (Fig. 1). Alteration of pegmatite yield to Chloritite-P, micaschist to Chloritite-M, and talc (Fig. 2) formed at the expense of the three lithologies (Moine et al., 1989; Parseval (de), 1992).

2.2 Sample characterization methods

2.2.1 Bulk rock characterization

Major and trace element concentrations were determined according to the analytical procedure developed by Carignan et al. (2001). Total CO_2 and sulfur have been measured using a HORIBA EMIA 320V2 analyzer. Organic carbon content has been measured using a HORIBA EMIA 320V2 analyzer on decarbonated samples after hydrochloric acid digestion of carbonates. For FeO, whole-rock samples have been digested by a sulpho-nitric solution, and Fe^{2+} content has been determined by volumetric titration. The latter consists of using a titrated potassium dichromate solution with potentiometric marking (platinum electrode and reference electrode Hg/Hg_2Cl_2, saturated KCl) of the equivalent point using an automatic Titroline Schott Titrimeter. Unfortunately, the digestion of most of the samples was incomplete, and Fe_2O_3 analyses corresponding to the total iron content of whole-rock samples will be used for diagrams and discussions. In contrast, FeO analyses will be presented for indicative purposes only. These whole rock analyses have been performed at Service d'Analyses des Roches et des Minéraux (SARM) at Centre de Recherche Pétrographiques et Géochimiques (CRPG), Nancy, France.

Qualitative and quantitative minerals composition of bulk samples were performed using X-ray powder diffraction (XRD) analysis on a Thermo X'TRA diffractometer working in Bragg-Brentano geometry. Powder diffraction analytical conditions involved an X-ray tube with a copper anode (CuKα – 1.54178 Å, voltage 45.2 kV, current 35 mA), the 0.9 mm divergence slit, and 1.6 mm anti-scatter slit were used on the primary side while on the secondary side, 1.6 mm anti-scatter slit and 0.3 mm receiving slit were used; soller slits 2.3˚ on both sides and a scintillation X-ray detector. Samples were scanned from 4 to 80˚2θ with step size 0.02˚2θ. Before the measurements, all samples were ground in a McCrone micronizing mill for 3 minutes. Mineral quantification was performed by the Rietveld refinement method using the BGMN program (www.bgmn.de), based on the XRD patterns collected on randomly oriented specimens for #CH4, #CH5, #CH6, #CH8, and #PORT7 samples, and on oriented specimens for #CH3 and #TLC1.

2.2.2 Whole Rock hydrogen isotope analysis

Hydrogen isotopic measurements of the different samples were performed online using the EA Eurovector – GV Isoprime IRMS System at CRPG laboratory (Nancy, France) according to the procedure developed by Lupker et al. (2012). First, the samples were weighed in tin capsules (1−5 mg). To remove atmospheric water potentially adsorbed by the samples,

these capsules were then loaded in a sample carousel and degassed at 120 ˚C under vacuum for 48h in a degassing canister (Lupker et al., 2012). After dehydration, the degassing canister was open into a dry, N_2 flushed glove box, and the sample carrousel was transferred into a sealed auto-sampler initially pre-flushed with He. The auto-sampler was then connected to the EA and pumped out for 20 min before opening it to the reduction column. Then, samples were combusted at 1450 ˚C on an EA glassy carbon reaction tube, filled with glassy carbon chips, and placed itself into a ceramic liner to reduce hydroxyls (OH) release by the samples into H_2. Produced gas was separated on a chromatographic column maintained at 60 ˚C, and H_2 was introduced into the mass spectrometer and analyzed for D/H isotopic composition. Isotopic compositions were determined by comparison with three internal standards routinely included during the analysis: (i) phlogopite (Mica-Mg: δD = -77 ‰), (ii) muscovite (MuscD65: δD = -85 ‰), (iii) fine-grained marine sediment from the Bay of Bengal (SO188: δD = -83 ‰). Produced H_2 was corrected from the H^{3+} contribution using in-house H_2 standard injections. The hydrogen isotopic composition is expressed as δD (‰) relative to Standard Mean Ocean Water (SMOW). The reproducibility of the method is better than 2‰ for δD.

2.2.3 Thermogravimetric (TG) analysis

Thermogravimetric (TG) analysis was performed using a TA Discovery instrument (TA Instruments, USA), which had a weight measurement accuracy of <0.1 μg, and a thermal drift between 200 and 1000˚C of <4 μg. A 20 mg air-dried powder sample placed in a Pt crucible was heated in a dry nitrogen gas atmosphere (>99.999 % purity) with a flow rate of 100 cm^3 min^{-1}. Before the TG experiment, each sample was dried in situ in the TG furnace isothermally for 15 min at 200 ˚C to remove the adsorbed water. A ramp heating to 1000 ˚C at a rate of 10 ˚C min^{-1} was used for each measurement. The total mass loss was calculated as the difference between mass loss recorded at 205 ˚C and 1000 ˚C (endpoint of heating). The thermal events temperature was analyzed using the first derivative of the TG curve (DTG).

The use of thermal analysis allows observing the thermal decomposition reactions, involving mostly dihydroxylation (in the range 400 ˚C – 800 ˚C). Dehydroxylation occurs during the heating of all phyllosilicates leading to the formation and migration of H_2O formed by neighbouring OH groups in the octahedral sheet (Heller-Kallai and Rozenson 1980; Drits et al. 1995).

2.3 Thermal treatment

Between 55 g to 80 g of the 0.5-5 mm grain size fraction of the rock samples were loaded in a pyrex tube, connected to the vacuum separation line (Fig.3), and pumped less than 1 minute at ambient temperature to reach good vacuo condition (~10^{-3} mbar). During

progressive heating to reach stationary temperatures, most of the condensable gases were released below 300°C (mainly adsorbed H_2O and CO_2) and were immediately trapped in liquid nitrogen. Fixed temperatures of 300 ˚C and 500 ˚C have been chosen for chloritite and talc samples, respectively, because preliminary tests revealed that non-condensable gases such as H_2 and CO were not released at lower temperatures. The progressively released non–condensable gases (H_2, CO) were regularly transferred in a calibrated volume using a Toepler pump (Fig. 3). All the samples were heated for about 20 hours, although most gases were released in the first hours. After 20 hours, the non-condensable gases were transferred in a sealed pyrex tube containing CuO and Cu_2O grains to be oxidized into H_2O and CO_2 for isotopic measurements (see section 2.4). Before being used, the CuO and Cu_2O grains were heated few minutes under vacuum at 350°C and pumped overnight at room temperature to remove adsorbed gases such as H_2O and CO_2. Finally, the condensable gases still trapped in the line were separated cryogenically. CO_2 was evacuated, and H_2O was collected using a clean syringe and transferred in a 2mL vial for isotopic analysis by CRDS (Cavity Ring Down Spectroscopy – see section 2.5.1).

2.4 Separation of H_2 and CO and quantification

After extraction, CO and H_2 are oxidized into CO_2 and H_2O with CuO and Cu_2O, respectively, at 450 ˚C for 1 hour. The produced CO_2 and H_2O are then separated cryogenically under vacuum. Water is then reduced into H_2 at 800 ˚C in a uranium furnace. H_2 and CO_2 are separately quantified using calibrated volume and transferred in a pyrex vessel for isotope analysis.

2.5 Hydrogen stable isotope analysis

2.5.1 H_2O

All water samples were analyzed at the CRPG UMR 7358 CNRS-UL (Nancy, France) using a CRDS L2140-i Picarro water isotope analyzer coupled to a A0211 vaporization module. Water released during thermal treatment of the rock samples was transferred into 2 mL Pyrex vials with a 0.1 mL conic insert and sealed by an ultraclean 9 mm septum. For each sample, 10 injections of 1.8 µL of water were performed. Only the 6 last injections were used for measurements to avoid any memory effect.

Isotopic compositions are reported in δ notation relative to the V-SMOW-SLAP scale. All samples were adjusted to three internal references calibrated on the international standards SLAP, GISP, and SMOW. Instrument precision was better than 0.1 ‰ and 1 ‰ for $\delta^{18}O$ and δD, respectively.

183 2.5.2 H_2 and CO

184 Hydrogen isotopic compositions of released H_2 were analyzed at the CRPG UMR 7358
185 CNRS-UL (Nancy, France) using a Dual-Inlet VG Isoprime Isotope Ratio Mass Spectrometer
186 (IRMS). Isotopic compositions are reported in δ notation relative to the V-SMOW-SLAP scale.
187 Two internal standards were analyzed, and each weekly batch of H_2 samples was obtained
188 following the same procedure of reducing uranium at 800 ˚C. Reproducibility for standards was
189 estimated to be lower than 2 ‰.

190 Carbon isotopic compositions of CO_2 formed by oxidation of CO (see section 2.4) were
191 analyzed at the CRPG UMR 7358 CNRS-UL (Nancy, France) using a Dual-Inlet VG Isoprime
192 Isotope Ratio Mass Spectrometer (IRMS). Isotopic compositions are reported in δ notation
193 relative to the V-PDB scale. Reproducibility is estimated to be lower than 0.2 ‰.
194
195
196 **3. Results**
197 **3.1 Chemical and mineral composition**

198 Three types of samples (chloritite-P, chloritite-M, and talc) have been sampled (Fig.
199 2). First, major elements composition shows that chlorites are magnesian-clinochlore (Table.
200 1) which is consistent with the nature of chlorite documented at Trimouns (Boutin, 2016;
201 Parseval (de), 1992). Compared to other chloritite samples, #CH3 and #CH8 are enriched in
202 SiO_2, depleted in MgO, and depleted in Al_2O_3 for the latter (Table 1). One can remark that
203 #CH5 is also slightly enriched in SiO_2 and slightly depleted in Al_2O_3. Based on XRD results
204 (Table 2), we can explain the major element concentrations in sample #CH3 by mixing with
205 quartz and muscovite and in sample #CH8 by a talc-chlorite mixture (chlorite ~11 % and talc
206 ~ 85 %). Regarding sample #CH5, the XRD results attest for a half-half mixing between
207 chlorite and talc.

208 Based on the work of Parseval (de) (1992) we used Cr, Ni, and V contents of chloritite
209 samples to determine their origins (i.e. derived from the alteration of pegmatoid or micaschist).
210 Cr, Ni, and V contents presented in Table 1 show that samples #CH4, #CH6, #CH10 and
211 #PORT-7 are pegmatoid-derived, whereas samples #CH3, #CH5, and #CH8 are micaschist-
212 derived. One could notice that the nickel content of samples #CH5 and #CH8 is slightly lower
213 than expected (~20 ppm whereas 25-60 ppm were expected) – a fact that could be explained by
214 mixing with significant quantities of talc, which is depleted in Ni (Table 1).

215 Finally, the total iron contents (expressed as Fe_2O_3) of chloritites and talc are low and
216 comparable to those documented in the literature (Parseval (de), 1992; Parseval (de) et al.,
217 1991) with values ranging from 1.43 wt% to 7.41 wt% for chloritites and of 0.42 wt% for talc.
218 As shown in Parseval (de) et al. (1991), Fe(III) in chlorite is located in tetrahedral sites only,

whereas Fe(II) is located in the three sites of the two octahedral sheets with most of the Fe(II) residing in the interlayer hydroxide sheet. Parseval (de) et al. (1991) showed that Fe(III) represents 20 to 30% of the total iron (Fe_2O_3), which is consistent with both the FeO (indicative purpose only) and the total iron content ($Fe_2O_{3)}$ documented for chloritite samples in the present study (Table 1). Villiéras et al. (1992) showed that very few Fe(II) was hosted by talc, the substitution of Mg by Fe(II) in the talc lattice being estimated at 1 %.

3.2 Whole-rock hydrogen isotope composition

Whole-rock hydrogen isotope compositions (Table 2) of studied samples are very homogeneous with values ranging between -48 ‰ and -43 ‰ with no specific variation related to the mineralogy of the samples.

3.3 Thermal evolution by thermogravimetry

The thermal behavior of all samples (except for #CH10) was tested using thermogravimetric (TG) analysis (Fig. 4). Under dynamic heating conditions, no significant mass change occurs below 500 ˚C, indicating no intense thermal decomposition reactions in this temperature range, which is consistent with TG results known for clinochlore (Lempart et al., 2018), talc (Čavajda et al., 2015), and muscovite (Mazzucato et al., 1999). The two-step (for chloritites) and one-step (for talc) rapid mass loss between 500 and 1000 ˚C is due to the dehydroxylation. The recorded total mass losses differed among all tested samples, resulting from different proportions of chlorite, talc, and muscovite (minerals that contributed to the weight loss on TG curves) and quartz. For the samples mainly containing chlorite: #CH4, #CH6, and #PORT7, the total mass losses range between 11.2 and 11.9 %, which are values close to the theoretical mass loss due to dehydroxylation of clinochlore (H_2O (+), 12-13 wt%; Lempart et al., 2018). The total mass losses are much lower for the other samples, and thermal events do not seem to be completed at 1000˚C. The dehydroxylation of talc-dominated samples, #CH8 and #TLC1, is represented by one DTG peak that is not completed up to 1000 ˚C, which is a common feature of talc (Čavajda et al., 2015). The complete dehydroxylation of talc requires a higher temperature, up to 1350 ˚C (Zhang et al. 2006). Chlorite-dominated samples (Fig. 4a, b, d, e, f) display two DTG peaks of mass loss with the maxima at ~600 ◦C and ~800 ◦C, which correspond to the dehydroxylation of the two octahedral sheets. The first peak is related to an interlayer (brucite) sheet, and the second to the octahedral sheet of the 2:1 layer (Lempart et al., 2020). Talc contributes to the latter thermal event due to its structural and chemical similarity and the 2:1 layer of clinochlore.

3.4 Thermal treatment

255 3.4.1 Stable isotope composition of interstitial/adsorbed water

256 As described in section 2.3, interstitial/adsorbed water is mainly released at a
257 temperature lower than 300 ˚C. It is immediately condensed in a liquid nitrogen trap to avoid
258 any exchange with H_2 released at a higher temperature. The released water was analyzed for its
259 hydrogen and oxygen stable isotopic composition. Data reported in Table 2 fall on, or very
260 close to, the Meteoric Global Water Line (Fig. 5). Only one water sample (#CH10) displays a
261 slightly lower isotopic composition in oxygen and hydrogen, suggesting that this sample
262 preserved meteoric water from another area (e.g. sampling area *vs* storage area).
263

264 3.4.2 Quantification and stable isotopic composition of released H_2 and CO

265 The quantities of H_2 and CO released during heating and the hydrogen stable isotopic
266 compositions of H_2 are correlated to the mineralogy of rock samples (Fig. 6a and 7a; Table 2).
267 The highest quantity of H_2 and CO are released from chloritite-P samples (4.7 to 7.4 ppm and
268 11.1 to 35.3 ppm, respectively), which are dominated by chlorite (> 85 %) with little talc (< 11
269 %) and few amounts of quartz (< 7 %). The lowest quantities of H_2 and CO are released from
270 the pure talc sample (> 98 % of talc): 0.7 ppm and 3.8 ppm, respectively. The amounts of H_2
271 and CO released from chloritite-M samples, constituted by ~10 to 50 % of chlorite, are
272 intermediate (0.5 to 1.7 ppm and 3 to 7 ppm, respectively). For H_2, a correlation between the
273 quantity of gas released, the nature of the sample, and the hydrogen isotopic composition is
274 observed (Fig. 6b). The lowest δD values (-258 ‰ to -224 ‰) are documented for chloritite-P
275 and the highest for talc (-140 ‰). The δD values of H_2 from chloritite-M are intermediate with
276 -183 ‰ and -160 ‰. For CO, $\delta^{13}C$ values are very homogeneous, ranging between -27.4 ‰
277 and -25.7 ‰ with no apparent correlation to the quantity of gas released (Fig. 7b). For CO and
278 H_2, no correlation is identified between the amount of gas released and the total iron content of
279 samples (Fig. 6c and 7c). However, a linear correlation is identified for chloritite-P (Fig. 6c).
280 Amounts of CO and H_2 released during experiments are not correlated between them (Fig. 7d).
281

282 **4. The origin(s) of H_2 release during thermal treatment of samples**

283 As presented in Figure 8, several processes can lead to the release of H_2 upon heating
284 of phyllosilicates. The question is whether the released H_2 was initially entrapped in our
285 samples or produced during the experiments.
286

287 **4.1 H_2 entrapped in minerals**

288 Recent studies demonstrated that physisorption of H_2 on phyllosilicates is possible
289 (Didier et al., 2012; Edge et al., 2014; Gil et al., 2009; Mondelli et al., 2015). However, all
290 these studies were performed under particular conditions (including low to cryogenic

temperatures, dry condition, pre-exposure to high H_2 pressure), making them difficult to extrapolate to the natural system. Truche et al. (2018) showed that H_2 is entrapped in clay-rich rocks naturally exposed to radiogenic H_2. In the alteration halo of the Cigar Lake U-deposit, H_2 produced by water radiolysis when in contact with U-minerals was trapped on clay minerals. The mechanism may be comparable to methane adsorption on shale.

For our study, the release of H_2 initially entrapped in the natural rock samples is unlikely. The main argument is related to the lack of H_2 release during progressive heating of the samples before reaching the stationary temperature of 300 ˚C for chloritite and 500 ˚C for talc (section 2.3). When reaching these temperatures, H_2 was not released abruptly but progressively. Compared to the release of H_2 documented by Truche et al. (2018) between 80 ˚C and 300 ˚C with a maximum flux of H_2 at ~200 ˚C, it is difficult to argue that H_2 released during our experiments was initially entrapped in the studied samples. The amount of H_2 released is also very different between the Truche et al. (2018) study and the present one: up to 500 ppm and 8 ppm, respectively. Moreover, our samples have been exposed to active pumping before heating for less than 1 min to reach vacuum condition in the extraction line (section 2.3), which could have extracted the hypothetical entrapped/adsorbed H_2.

4.2 Reduction of H_2O by Fe(II) oxidation

One can envision that H_2 production resulted from the reduction of adsorbed/interstitial H_2O, initially contained in the rock samples, associated with Fe(II) oxidation contained in chlorite. Alternatively, the production of H_2 could have been formed by the same process, but from H_2O formed at higher temperatures during the dehydroxylation stage of the rock (Villiéras et al., 1992). The generalized reaction can be represented according to:

$$2FeO + H_2O \rightarrow Fe_2O_3 + H_2 \quad (1)$$

The first hypothesis, involving the reduction of H_2O initially entrapped in the rock samples, is very unlikely for the following reasons. A time/temperature gap exists between the release of adsorbed/interstitial H_2O occurring at T < 300 ˚C and the subsequent H_2 release occurring at 300 ˚C (for chloritite) and 500 ˚C (for talc). Moreover, the experiments were performed under vacuum conditions, and a liquid nitrogen trap was emplaced since the beginning of the experiments to remove the adsorbed/interstitial H_2O upon heating (Fig. 3). The low-temperature release, combined with the quick transfer and trapping of H_2O, makes very unlikely the possibility to reduce water by oxidizing structural Fe(II). In comparison, H_2 production related to experimental serpentinization of olivine grains is kinetically hindered at T<300 ˚C. Several hundreds of hours are required to produce detectable amount of H_2 at T > 200°C (McCollom et al., 2016). Finally, the stable isotopic compositions (O and H) of retrieved

328 waterfall lie perfectly on the GMWL (Fig. 5). If H_2 release would be related to the reduction of
329 H_2O, their isotopic compositions should be in isotopic equilibrium. For δD_{H2O} values between
330 -100 ‰ and -60 ‰ (Table 2, Fig. 5), the hydrogen isotopic composition of H_2 should be
331 between ~ -615 ‰ and -575 ‰ at 300 ˚C and between -420 ‰ and -380 ‰ at 500 ˚C (Bottinga,
332 1969).
333 The second hypothesis considers the reduction of H_2O formed during dehydroxylation
334 of the rock by oxidizing Fe(II) contained in chlorite. Dehydroxylation is a high-temperature
335 process occurring in a broad range of temperatures for trioctahedral phyllosilicates (Fig. 8),
336 from 400 to 850 ˚C for chlorites (Lempart et al., 2018) and from 750 to 1100 ˚C for talc (Zhang
337 et al., 2006). This process consists of a reaction between hydroxyl groups (OH) forming water
338 molecules (Drits et al., 1995; Drits et al., 2012a; Drits et al., 2012b; Guggenheim et al., 1987;
339 Vedder and Wilkins, 1969):
340

$$(OH)_{2n} \rightarrow nH_2O + nO_r \quad (2)$$

341
342 where O_r is the residual oxygen in the structure.
343 The newly formed H_2O could oxidize structural Fe(II) and form H_2 by reducing H_2O following
344 the equation (1) as proposed by Villiéras et al. (1992) to explain the release of H_2 during heating
345 of talc and chloritite from Trimouns. In this latter study, the authors also followed the method
346 of Zimmermann et al. (1988) to recover and separate the different gases released at various
347 temperature steps (talc: from 200 to 1100 ˚C; chloritite from pegmatite: from 280 to 1100 ˚C;
348 chloritite from micaschist: from 300 to 1080 ˚C). The authors documented H_2 release, between
349 0.01 and 0.8 ppm, at low temperature (between 200 and 300 ˚C) for chloritite and talc. The
350 release of H_2 reached a maximum at 600 ˚C and 850 ˚C for chloritite and talc, respectively,
351 with values of several tens of ppm. The main conclusion of Villiéras et al. (1992) was that H_2
352 was formed by reduction of H_2O, released during dehydroxylation, and concomitant oxidation
353 of Fe(II) to Fe(III) contained in the minerals following the equations (1). However, this
354 conclusion only explains the significant release of H_2 at a temperature above 450 ˚C and 750
355 ˚C (Fig. 8) for chloritite and talc, respectively. Thus, the question of the origin of H_2 released
356 at a temperature lower than 450 ˚C remains open.
357 Here, the experiments have been performed at temperatures significantly lower than
358 those expected to initiate dehydroxylation (see section 3.2). Consequently, it is improbable to
359 explain the release of H_2 by reducing H_2O formed during dehydroxylation on structural Fe(II).
360
361 **4.3 H_2 produced by dehydrogenation and significance of δD_{H2} values**

Dehydroxylation and dehydrogenation are competitive processes that can co-occur in a similar range of temperatures and produce H_2O and H_2 gas independently (Lempart et al., 2018; Lempart et al., 2020).

Dehydrogenation is a thermally induced reaction overlapping with dehydroxylation. One proposed reaction mechanism proceeds by a release of one hydroxyl hydrogen atom per one oxidized Fe(II) atom octahedrally coordinated with OH groups, leading to the generation of H_2 (Brindley and Youell 1952; MacKenzie and Berezowski 1984):

$$Fe(II) + OH\text{-} \rightarrow Fe(III) + O^{2\text{-}}_{r} + H^{\bullet}\uparrow \quad (3)$$

The dehydrogenation process was observed for all Fe(II)-containing phyllosilicates and was thoroughly described for biotites, amphibolites (Vedder and Wilkins 1969; Rouxhet et al. 1972; Sanz et al. 1983), and/or chlorites (Borggaard et al. 1982; Steudel et al. 2016; Lempart et al. 2018). The dehydrogenation occurs under an inert and oxidizing gas atmosphere or vacuum conditions and prefers long-term heating over fast ramp heating conditions (Lempart et al., 2018; Rouxhet et al., 1972; Sanz et al., 1983; Vedder and Wilkins, 1969). For chamosite, dehydrogenation was observed at a temperature as low as 350°C during isothermal heating, whereas for Fe(II)-poor clinochlore temperature of dehydrogenation was between 400-450 ˚C (Lempart et al., 2018; Lempart et al., 2020) (Fig. 8). However, such results were tested by using an inert carrier gas during thermogravimetry analysis that only allows tracking relatively high mass loss, mostly related to dehydroxylation. Hence, traces of hydrogen released at lower temperatures are not detectable by that method.

Although the formation of H_2 upon heating of Fe(II)-rich phyllosilicates is indisputable, it is also documented in some studies concerning iron-poor minerals. Several studies showed that the release of hydrogen upon heating in vacuo of kaolinite occurs only in the course of, or after, dehydroxylation (Heide and Földvari, 2006; Heller-Kallai, 1997). Detailed mechanisms remain, however, obscure. Some authors suggested that H_2 production depends on structural properties, such as the specific arrangement of OH-ions and formation of lattice vacancies, making possible the reaction between residual OH- groups as follow (Heide and Földvari, 2006; Heller-Kallai, 1997):

$$OH^{-} + OH^{-} \rightarrow 2O^{-} + H_2 \quad (4)$$

However, the conclusions proposed by Heide and Földvari (2006) and Heller-Kallai (1997) were also partially questioned by the study of Lempart et al. (2020) where H_2 release was attributed only to oxidative dehydrogenation. Lempart et al. (2020) also challenged these

conclusions by showing the absence of H_2 generation during the heating of the same kaolinite as tested by Heide and Földvari (2006) and Heller-Kallai (1997) in an inert gas atmosphere.

In the present study, H_2 release is documented at a temperature significantly lower than those required to reach dihydroxylation, but dehydrogenation has also been reported at lower temperatures, between 350 ˚C and 450 ˚C, even for clinochlore (Lempart and Derkowski, 2019; Lempart et al., 2018; Lempart et al., 2020). The samples used in this work are relatively iron-poor clinochlore, but the few ppm of H_2 released may be consistent with structural Fe(II) oxidation. Indeed, precisely for chloritite-P, the purest chloritite samples, a correlation between the quantities of H_2 released and the total iron content is observed (Fig. 6c). Thus, these results suggest that the dehydrogenation probably produced H_2 during our experiments.

From an isotopic point of view, δD_{H2} values are significantly lower than the very homogeneous δD values around -45 ‰ for chloritite and talc whole-rock samples (Table 2). These values could suggest that large hydrogen isotope fractionations occur during the formation of H_2 by dehydrogenation. The correlation between the quantity of H_2 released during the experiments and the δD_{H2} values could suggest that this fractionation evolves with the intensity of dehydrogenation and the mineralogy of the starting material (Fig. 6b).

This hydrogen isotope fractionation associated with dehydrogenation has also been documented by Feeley and Sharp (1996) who have shown that biotite having experienced dehydrogenation have high δD values compared to the initial material. The released H_2 is consequently supposed to have low δD values compared to the starting material. These conclusions are consistent with our observations and should deserve additional investigation to determine the effect of the nature of the mineral, the temperature, and the rates of dehydrogenation on the hydrogen isotope fractionation between OH-rich minerals and released H_2.

5. The origin of CO

As for H_2, CO could have been initially entrapped in the natural rock or produced during experiments. However, it is unlikely that CO could have been initially entrapped in our samples for the same reasons as H_2 (active pumping before heating and lack of CO during progressive heating). Carbon monoxide formed by reducing adsorbed/interstitial CO_2 on structural Fe(II) following the equation (5) is also unlikely.

$$2FeO + CO_2 \rightarrow Fe_2O_3 + CO \quad (5)$$

As for H_2O, the low-temperature release of CO_2 and its quick transfer and trapping in a liquid nitrogen trap make very unlikely the possibility to reduce CO_2 by oxidizing structural Fe(II) (see section 4.2). An alternative hypothesis could consist in reducing CO_2 formed by decarbonation of samples as proposed by Villiéras et al. (1992) for similar talc and chloritite samples from the Trimouns deposit. However, decarbonation is a high-temperature process that consists of the thermal decomposition of carbonate at a temperature above 600°C (Sharp et al., 2003), significantly higher than the temperature of our experiments.

Even if the origin of CO released at 300 °C remains enigmatic, we suggest that CO could be derived from a process involving the graphite contained in few amounts in talc and chlorite samples from the deposit (Table.1, Parseval (de), 1992). Indeed, the carbon isotope compositions of CO released in this study are exceptionally homogeneous between -27.4 ‰ to -25.7 ‰ (Table 2) and very close to the $\delta^{13}C_{Graphite}$ value of -24.4 ‰ documented from whole rock analysis of Chlorite-P (Parseval (de), 1992).

6. Conclusion and perspectives

In this study, we document H_2 and CO release during heating of talc and chloritite from the Trimouns deposit at 300 and 500°C, respectively. If the origin of CO remains enigmatic but could be linked to reaction with graphite, we propose that H_2 has been produced during the experiments by dehydrogenation of the starting material. Very low δD_{H2} values compared to the initial δD values of sampled material are documented and question the isotopic fractionations that dehydrogenation could induce. This extensive hydrogen isotopic fractionation between OH-rich minerals and produced H_2 during dehydrogenation would deserve further investigations to fully understand the effects of mineral composition, temperature, and the rates of dehydrogenation. An important recommendation from this work is that thermal degassing of rocks must be performed at a temperature lower than 300 °C to ensure the absence of dehydrogenation of clays and in situ generations of H_2 and CO. Finally, dehydrogenation may occur in various magmatic-metamorphic-hydrothermal environments and should be accounted for as a potential H_2 source term in the hydrogen geochemical cycle. The isotopic signature of H_2 produced by dehydrogenation has to be better constrained to evaluate the geological significance of this process.

ACKNOWLEDGEMENTS

Aurélien Randi, Catherine Lorgeoux and, Gilles Bessaque are warmly thanked for their precious technical help during the first steps of the study. Alexandre Boutin, Michel de Saint Blanquat, and Philippe de Parseval are thanked for their support in the fieldwork as experts of

the area. This work was conducted under the framework of a CREGU contract, the “Fluids” program on Pyrenees, financed by the TotalEnergies company. L. Truche acknowledges support from the Institut Universitaire de France

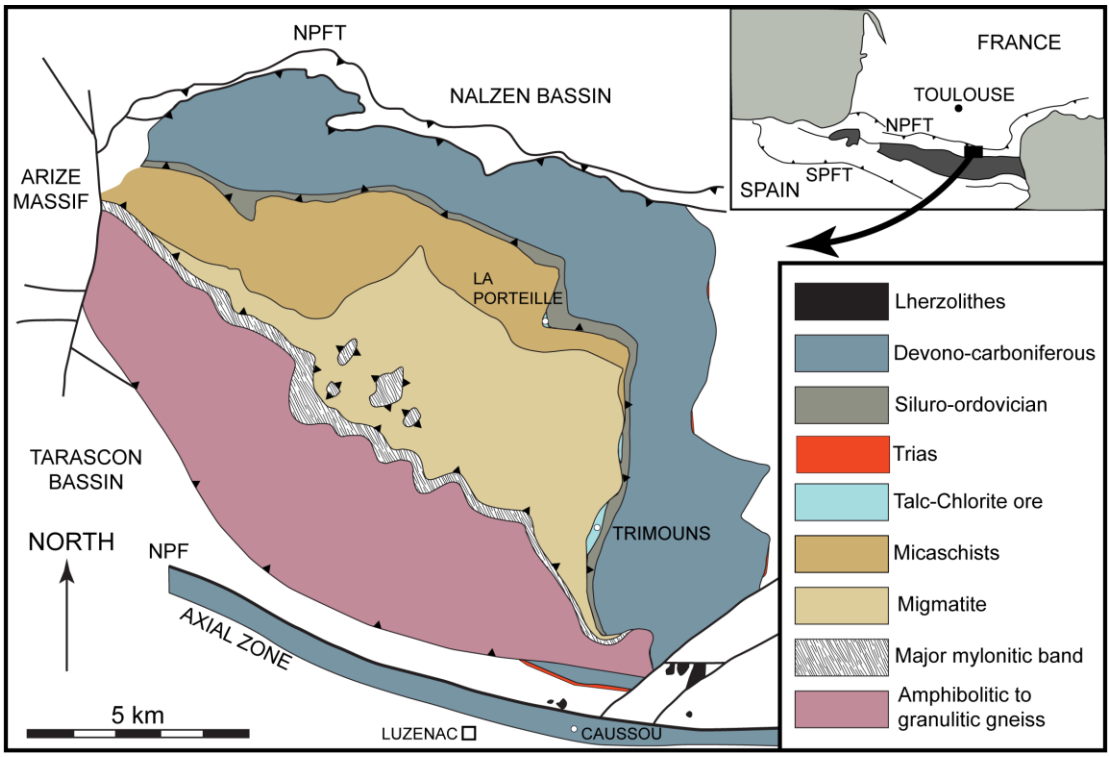

Figure 1 Simplified geological map of the Saint Barthelemy Massif modified after Boutin et al. (2016) and Saint Blanquat (de) (1989)

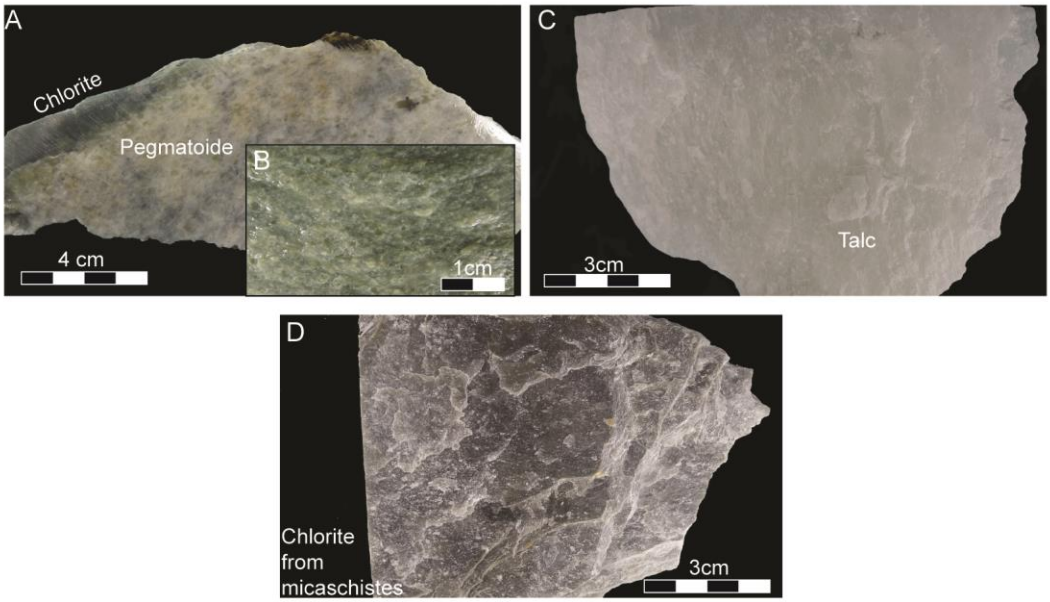

Figure 2 Photos of the three types of samples studied in this work. A, B: samples #CH10 and #CH4, chloritite-P with their typical light green color; C: sample #TLC1, talc with its characteristic white color; D: sample #CH5, chloritite-M with its dark green-black color

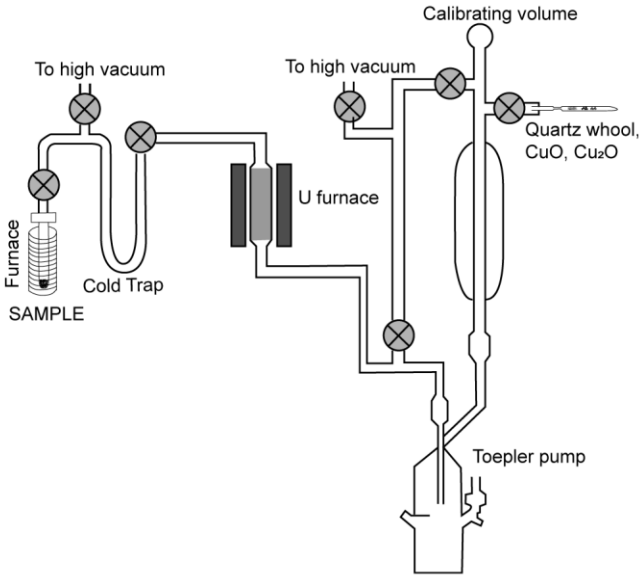

Figure 3 Schematic diagram of the extraction and separation line inspired from Zimmermann et al. (1988)

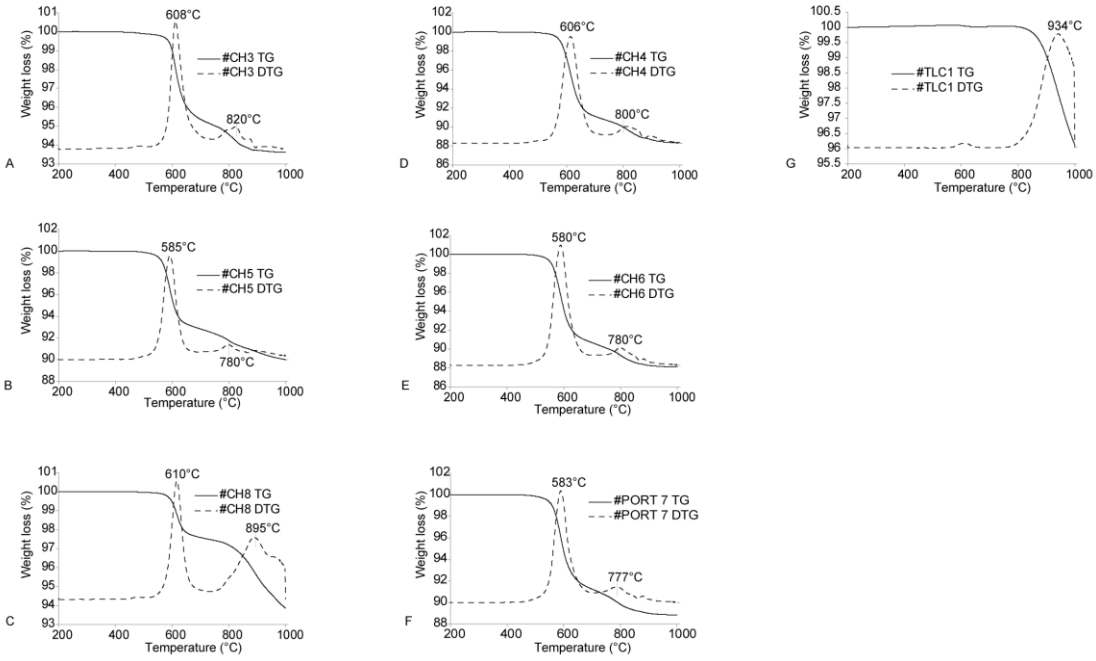

Figure 4 Thermogravimetric (TG) pattern of studied samples ramp heated with a 10 ˚C/min rate to 1000 ˚C under N_2 gas.

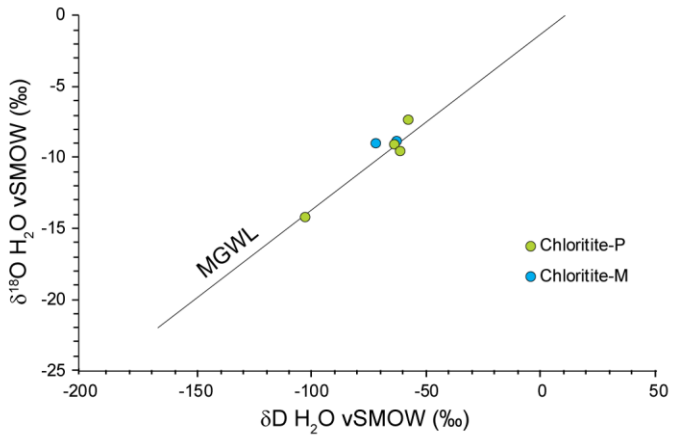

Figure 5 Oxygen and hydrogen isotope compositions of adsorbed/entrapped water released from chloritite-P and chloritite-M samples during the first heating steps. Meteoric Global Water Line (MGWL) has been drawn using the following equation: $\delta D = 8 \times \delta^{18}O + 10$

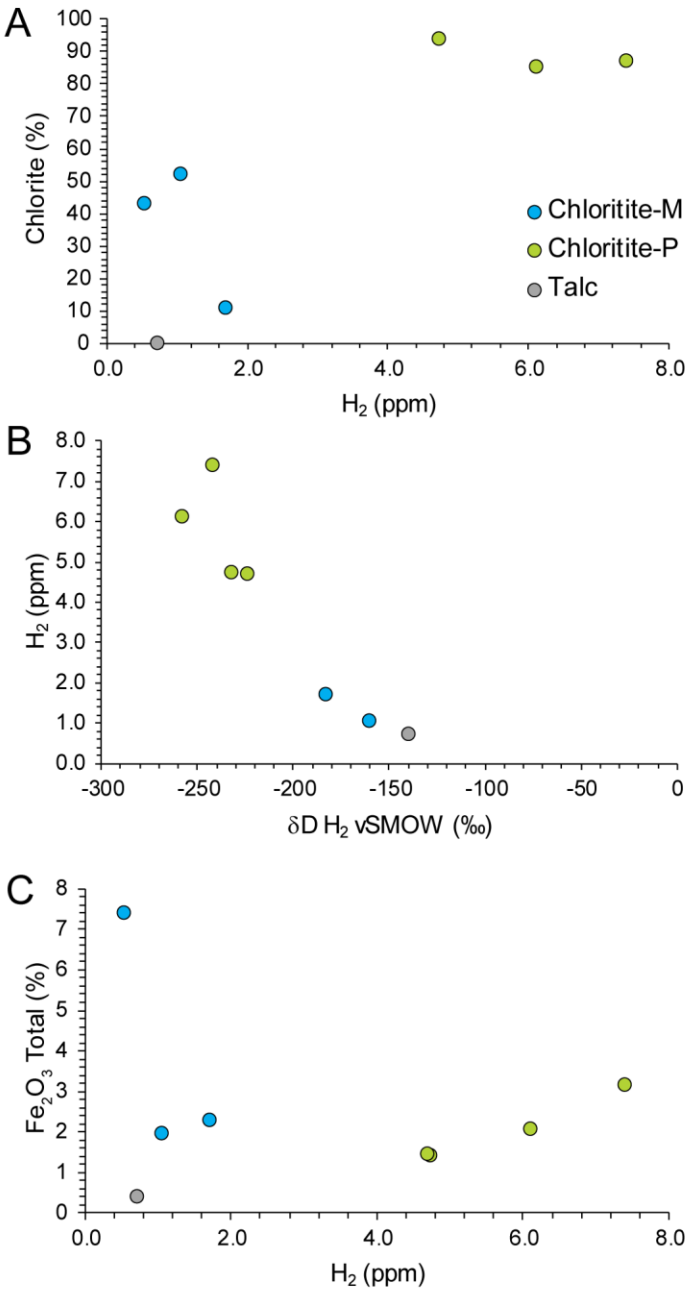

Figure 6 A: Quantity of H_2 released during experiments as a function of the mineralogy of the sample. The chlorite amount is given in Table 2, based on XRD analyses of rock samples. B: Hydrogen isotopic composition of H_2 as a function of the quantity of H_2 released during experiments. C: Quantity of H_2 released during experiments as a function of the total iron content of the sample.

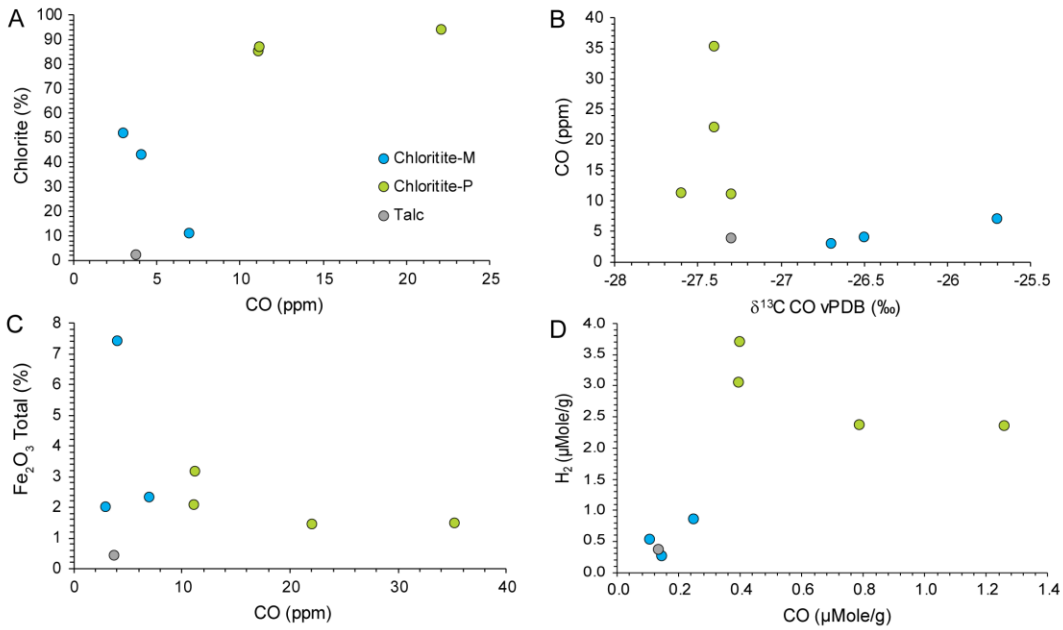

Figure 7 A: Quantity of CO released during experiments as a function of the mineralogy of the sample. The chlorite proportions are given in Table 2 based on XRD analyses of rock samples. B: Carbon isotopic composition of CO as a function of the quantity of CO released during experiments. C: Quantity of CO as a function of the total iron content of the sample. D: Quantity of CO as a function of the quantity of H_2 released during experiments.

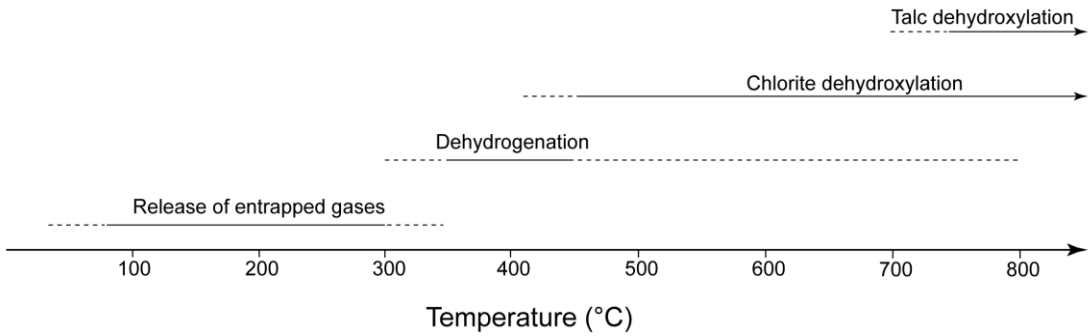

Figure 8 Sketch summarizing the range of temperatures in which various gas producer processes are likely to occur. See text for details.

Sample		#CH3	#CH5	#CH8	#CH4	#CH6	#CH10	#PORT-7	#TLC1
Lithology		Chloritite-M	Chloritite-M	Chloritite-M	Chloritite-P	Chloritite-P	Chloritite-P	Chloritite-P	Talc
SiO_2	%	42.53	38.36	54.45	33.28	34.28	33.64	31.72	62.00
Al_2O_3	%	17.26	14.26	3.68	18.53	16.71	17.25	18.12	0.23
Fe_2O_3	%	7.41	1.99	2.31	2.08	1.43	1.46	3.17	0.42
MnO	%	0.05	B.D.L.	B.D.L.	0.02	B.D.L.	B.D.L.	0.02	B.D.L.
MgO	%	21.91	32.86	29.89	32.94	33.44	33.59	33.38	31.69
CaO	%	0.09	0.23	1.01	0.56	1.02	1.15	0.36	0.20
Na_2O	%	B.D.L.	B.D.L.	B.D.L.	B.D.L.	B.D.L.	B.D.L.	B.D.L.	B.D.L.
K_2O	%	0.17	B.D.L.	B.D.L.	B.D.L.	B.D.L.	B.D.L.	B.D.L.	B.D.L.
TiO_2	%	0.78	0.84	0.11	0.07	B.D.L.	B.D.L.	0.03	B.D.L.
P_2O_5	%	B.D.L.	0.16	0.79	0.43	0.77	0.87	0.26	B.D.L.
LOI	%	9.41	10.97	7.56	12.16	11.99	12.20	12.94	5.31
Total	%	99.60	99.67	99.80	100.07	99.64	100.16	100.00	99.85
CO_2 total	%	0.56	0.23	4.99	0.02	0.07	0.13	0.04	0.14
C_{org}	%	0.13	0.06	1.37	<0.01	<0.01	<0.01	<0.01	0.01
FeO	%	6.16*	1.68*	1.72*	1.67*	1.18*	1.19	2.45	0.32
S total	%	<0.01	0.03	0.03	<0.01	<0.01	<0.01	<0.01	<0.01
As	ppm	0.84	B.D.L.	B.D.L.	B.D.L.	B.D.L.	B.D.L.	B.D.L.	B.D.L.
Ba	ppm	25.08	B.D.L.	B.D.L.	B.D.L.	B.D.L.	B.D.L.	B.D.L.	B.D.L.
Be	ppm	1.35	2.62	0.43	1.89	2.13	2.30	2.24	0.17
Bi	ppm	B.D.L.	0.07	B.D.L.	B.D.L.	B.D.L.	B.D.L.	B.D.L.	B.D.L.
Cd	ppm	B.D.L.	0.03	B.D.L.	0.03	0.08	0.15	B.D.L.	B.D.L.
Ce	ppm	61.57	0.91	1.72	9.25	2.51	2.31	1.49	0.08
Co	ppm	11.52	1.94	2.96	1.57	0.80	1.90	3.61	0.70
Cr	ppm	87.08	68.60	30.04	0.73	B.D.L.	0.67	B.D.L.	B.D.L.
Cs	ppm	1.88	1.65	0.57	1.00	1.59	1.79	2.66	0.20
Cu	ppm	B.D.L.	B.D.L.	B.D.L.	B.D.L.	2.03	2.56	3.18	B.D.L.
Dy	ppm	2.64	0.37	0.57	1.41	7.66	5.49	0.85	0.02
Er	ppm	1.46	0.32	0.24	0.69	4.04	3.01	0.43	0.01
Eu	ppm	0.31	0.02	0.08	0.08	0.46	0.30	0.05	B.D.L.
Ga	ppm	22.37	20.37	5.60	22.18	21.30	21.70	25.18	0.34
Gd	ppm	3.30	0.27	0.62	1.17	4.12	2.78	0.56	0.01
Ge	ppm	1.30	0.87	2.01	1.04	0.87	0.82	0.77	1.54
Hf	ppm	4.08	6.54	0.51	1.75	1.59	1.24	1.96	B.D.L.
Ho	ppm	0.53	0.10	0.11	0.27	1.61	1.18	0.17	0.00
In	ppm	B.D.L.	B.D.L.	B.D.L.	B.D.L.	B.D.L.	B.D.L.	B.D.L.	B.D.L.
La	ppm	30.65	0.39	0.71	4.38	0.79	0.78	0.55	0.04
Lu	ppm	0.24	0.10	0.02	0.11	0.30	0.24	0.05	0.00
Mo	ppm	B.D.L.	B.D.L.	29.43	B.D.L.	B.D.L.	B.D.L.	B.D.L.	B.D.L.
Nb	ppm	12.83	14.00	2.88	15.01	69.44	40.83	16.16	0.09
Nd	ppm	25.61	0.59	1.61	4.49	3.25	2.36	1.23	0.05
Ni	ppm	43.88	20.19	19.33	6.13	5.63	6.09	7.88	6.47
Pb	ppm	0.49	B.D.L.	1.06	B.D.L.	1.68	1.94	1.24	B.D.L.
Pr	ppm	7.05	0.13	0.31	1.15	0.50	0.40	0.24	0.01
Rb	ppm	5.23	0.94	0.34	0.91	1.26	1.71	0.74	0.30
Sc	ppm	14.96	12.54	2.11	5.53	3.01	3.09	3.73	B.D.L.
Sb	ppm	B.D.L.	B.D.L.	0.08	B.D.L.	B.D.L.	B.D.L.	B.D.L.	B.D.L.
Sm	ppm	4.60	0.21	0.54	1.20	2.41	1.59	0.46	0.01
Sn	ppm	5.91	20.31	1.65	2.31	6.47	6.63	8.94	0.32
Sr	ppm	1.29	1.19	3.02	1.67	3.75	4.07	1.40	B.D.L.
Ta	ppm	1.30	1.25	0.94	4.49	106.27	45.70	7.16	0.12
Tb	ppm	0.45	0.05	0.10	0.23	1.05	0.74	0.12	0.00
Th	ppm	15.07	13.19	2.68	1.58	0.73	0.86	0.53	0.02
Tm	ppm	0.22	0.06	0.03	0.11	0.52	0.39	0.06	0.00
U	ppm	2.91	3.11	20.05	5.98	42.56	43.03	3.69	0.02
V	ppm	98.14	85.79	47.80	2.69	7.67	7.84	15.35	1.38
W	ppm	27.64	22.31	7.57	2.78	12.35	4.83	B.D.L.	B.D.L.
Y	ppm	13.60	2.61	2.86	6.70	25.82	19.22	2.94	0.11
Yb	ppm	1.51	0.50	0.17	0.77	2.76	2.18	0.37	0.01
Zn	ppm	51.10	B.D.L.	24.97	12.59	B.D.L.	B.D.L.	11.65	B.D.L.
Zr	ppm	148.19	252.95	20.13	39.27	18.23	14.69	32.62	B.D.L.

519 * Incomplete dissolution, indicative value of FeO content

520 **Table 1** Major and trace element concentrations of studied samples

Sample	#CH3	#CH5	#CH8	#CH4	#CH6	#CH10	#PORT-7	#TLC1
Lithology	Chloritite-M	Chloritite-M	Chloritite-M	Chloritite-P	Chloritite-P	Chloritite-P	Chloritite-P	Talc
H_2 (ppm)	0.5	1.1	1.7	6.1	4.7	4.7	7.4	0.7
s		0.1	0.4	0.2	0.3	0.1	0.5	0.0
n	1	2	2	2	2	2	2	2
δD_{H2} vs. vSMOW (‰)	n/a	-160	-183	-258	-232	-224	-242	-140
s		11	13	3	3	5		
n		2	2	2	2	2	1	1
CO (ppm)	4.1	3	7	11.1	22.1	35.3	11.2	3.8
s		0.2	1.6	0	3.7	0.2	0.4	0.7
n	1	2	2	2	2	2	2	2
$\delta^{13}C$ CO vs. vSMOW (‰)	-26.5	-26.7	-25.7	-27.3	-27.4	-27.4	-27.6	-27.3
s		0.6	0.9	0.2	0.1	0.1	0.2	0
n	1	2	2	2	2	2	2	2
δD_{H2O} vs. vSMOW (‰)	n/a	-62	-71	-63	-57	-102	-61	n/a
s		0		4		4	5	
$\delta^{18}O_{H20}$ vs. vSMOW (‰)	n/a	-8.9	-9.1	-9.1	-7.4	-14.3	-9.6	n/a
s		0.0		0.5		0.3	0.7	
n		2	1	2	1	2	2	
δD_{WR} vs. vSMOW (‰)	-48	-45	-47	-48	-46	-44	-45	-43
Chlorite (%)	43	52	11	85	94	n/a	87	<2
Talc (%)	2	44	85	11	5	n/a	6	98
Quartz (%)	35	4	<2	4	<2	n/a	7	
Muscovite (%	20							

Table 2 Amounts of H_2 and CO released during experiments, and stable isotope compositions of H_2 (δD_{H2}), interstitial/adsorbed H_2O (δD_{H2O}, $\delta^{18}O_{H2O}$), CO ($\delta^{13}C_{CO}$). Hydrogen isotope compositions of whole-rock chloritite and talc samples (δD_{WR}). XRD quantitative estimation of mineral compositions of whole-rock samples. n: number of replicates; σ: Difference between the average and the replicates; n/a: not available.

REFERENCES

Boiron, M.C., Boulvais, P., Cathelineau, M., Banks, D.A., Calvayrac, N. and Hubert, G. (2005) Fluid circulation at the origin of the Trimouns talc deposit (Pyrenees, France), ECROFI XVIII, Siena.

Boiron, M.C., Cathelineau, M., Dubessy, J., Fabre, C., Boulvais, P. and Banks, D.A. (2007) Na Ca-Mg rich brines and talc formation in the giant talc deposit of Trimouns (Pyrénées): fluid inclusion chemistry and stable isotope study, European Current Research on Fluid Inclusions (ECROFI-XIX) University of Bern, Switzerland.

Bottinga, Y. (1969) Calculated fractionation factors for carbon and hydrogen isotope exchange in the system calcite-carbon dioxide-graphite-methane-hydrogen-water vapor. Geochimica et Cosmochimica Acta 33, 49-64.

Boulvais, P., de Parseval, P., D'Hulst, A. and Paris, P. (2006) Carbonate alteration associated with talc-chlorite mineralization in the eastern Pyrenees, with emphasis on the St. Barthelemy Massif. Mineralogy and Petrology 88, 499-526.

Boutin, A. (2016) Etude des conditions de formation du gisement de talc-chlorite de Trimouns, Géosciences Environnement Toulouse (GET), UMR 5563. Université de Toulouse III, Paul Sabatier, p. 264.

Boutin, A., de Saint Blanquat, M., Poujol, M., Boulvais, P., de Parseval, P., Rouleau, C. and Robert, J.-F. (2016) Succession of Permian and Mesozoic metasomatic events in the eastern Pyrenees with emphasis on the Trimouns talc–chlorite deposit. International Journal of Earth Sciences 105, 747-770.

Busch, A., Bertier, P., Gensterblum, Y., Rother, G., Spiers, C.J., Zhang, M. and Wentinck, H.M. (2016) On sorption and swelling of CO2 in clays. Geomechanics and Geophysics for Geo-Energy and Geo-Resources 2, 111-130.

Carignan, J., Hild, P., Mevelle, G., Morel, J. and Yeghicheyan, D. (2001) Routine Analyses of Trace Elements in Geological Samples using Flow Injection and Low Pressure On-Line Liquid Chromatography Coupled to ICP-MS: A Study of Geochemical Reference Materials BR, DR-N, UB-N, AN-G and GH. Geostandards Newsletter 25, 187-198.

Čavajda, V., Uhlík, P., Derkowski, A., Čaplovičova, M., Madejová, J., Mikula, M. and Ifka, T. (2015) Influence of Grinding and Sonication on the Crystal Structure of Talc. Clays and Clay Minerals 63, 311-327.

Didier, M., Leone, L., Greneche, J.-M., Giffaut, E. and Charlet, L. (2012) Adsorption of Hydrogen Gas and Redox Processes in Clays. Environmental Science & Technology 46, 3574-3579.

Drits, V.A., Besson, G. and Muller, F. (1995) An Improved Model for Structural Transformations of Heat-Treated Aluminous Dioctahedral 2:1 Layer Silicates. Clays and Clay Minerals 43, 718-731.

Drits, V.A., Derkowski, A. and McCarty, D.K. (2012a) Kinetics of partial dehydroxylation in dioctahedral 2:1 layer clay minerals. American Mineralogist 97, 930-950.

Drits, V.A., McCarty, D.K. and Derkowski, A. (2012b) Mixed-layered structure formation during trans-vacant Al-rich illite partial dehydroxylation. American Mineralogist 97, 1922-1938.

575 Edge, J.S., Skipper, N.T., Fernandez-Alonso, F., Lovell, A., Srinivas, G., Bennington, S.M.,
576 Garcia Sakai, V. and Youngs, T.G.A. (2014) Structure and Dynamics of Molecular Hydrogen
577 in the Interlayer Pores of a Swelling 2:1 Clay by Neutron Scattering. The Journal of Physical
578 Chemistry C 118, 25740-25747.

579 Feeley, T.C. and Sharp, Z.D. (1996) Chemical and hydrogen isotope evidence for in situ
580 dehydrogenation of biotite in silicic magma chambers. Geology 24, 1021-1024.

581 Gil, A., Trujillano, R., Vicente, M.A. and Korili, S.A. (2009) Hydrogen adsorption by
582 microporous materials based on alumina-pillared clays. International Journal of Hydrogen
583 Energy 34, 8611-8615.

584 Guggenheim, S., Chang, Y.-H. and Koster van Groos, A.F. (1987) Muscovite
585 dehydroxylation; high-temperature studies. American Mineralogist 72, 537-550.

586 Heide, K. and Földvari, M. (2006) High temperature mass spectrometric gas-release studies
587 of kaolinite Al2[Si2O5(OH)4] decomposition. Thermochimica Acta 446, 106-112.

588 Heller-Kallai, L. (1997) The nature of clay volatiles and condensates and the effect on their
589 environment. Journal of thermal analysis 50, 145-156.

590 Klewiah, I., Berawala, D.S., Alexander Walker, H.C., Andersen, P.Ø. and Nadeau, P.H.
591 (2020) Review of experimental sorption studies of CO2 and CH4 in shales. Journal of Natural
592 Gas Science and Engineering 73, 103045.

593 Lempart, M. and Derkowski, A. (2019) Hydrogen liberation during heating of phyllosilicates,
594 Book of abstracts, EuroClay 2019, Paris, p. 385.

595 Lempart, M., Derkowski, A., Luberda-Durnaś, K., Skiba, M. and Błachowski, A. (2018)
596 Dehydrogenation and dehydroxylation as drivers of the thermal decomposition of Fe-
597 chlorites. American Mineralogist 103, 1837-1850.

598 Lempart, M., Derkowski, A., Strączek, T. and Kapusta, C. (2020) Systematics of H2 and H2O
599 evolved from chlorites during oxidative dehydrogenation. American Mineralogist 105, 932-
600 944.

601 Lupker, M., France-Lanord, C., Galy, V., Lavé, J., Gaillardet, J., Gajurel, A.P., Guilmette, C.,
602 Rahman, M., Singh, S.K. and Sinha, R. (2012) Predominant floodplain over mountain
603 weathering of Himalayan sediments (Ganga basin). Geochimica et Cosmochimica Acta 84,
604 410-432.

605 Mazzucato, E., Artioli, G. and Gualtieri, A. (1999) High temperature dehydroxylation of
606 muscovite-2M1: a kinetic study by in situ XRPD. Physics and Chemistry of Minerals 26, 375-
607 381.

608 McCollom, T.M., Klein, F., Robbins, M., Moskowitz, B., Berquó, T.S., Jöns, N., Bach, W.
609 and Templeton, A. (2016) Temperature trends for reaction rates, hydrogen generation, and
610 partitioning of iron during experimental serpentinization of olivine. Geochimica et
611 Cosmochimica Acta 181, 175-200.

612 Moine, B., Fortune, J.P., Moreau, P. and Viguier, F. (1989) Comparative mineralogy,
613 geochemistry, and conditions of formation of two metasomatic talc and chlorite deposits;
614 Trimouns (Pyrenees, France) and Rabenwald (Eastern Alps, Austria). Economic Geology 84,
615 1398-1416.

Mondelli, C., Bardelli, F., Vitillo, J.G., Didier, M., Brendle, J., Cavicchia, D.R., Robinet, J.-C. and Charlet, L. (2015) Hydrogen adsorption and diffusion in synthetic Na-montmorillonites at high pressures and temperature. International Journal of Hydrogen Energy 40, 2698-2709.

Parseval (de), P. (1992) Étude minéralogique et géochimique du gisement de talc et chlorite de Trimouns. Université de Toulouse III.

Parseval (de), P., Fournes, L., Fortune, J.P., Moine, B. and Ferret, J. (1991) Distribution du fer dans les chlorites par spectrométrie Mössbauer (57Fe) : Fe(III) dans les chlorites du gisement de talc-chlorite de Trimouns (Pyrénées, France). C.R. Acad. Sci. II 312, 1321-1326.

Parseval (de), P., Jiang, S., Fontan, F., Wang, R., Martin, F. and Freeet, J. (2004) Geology and ore genesis of the Trimouns talc chlorite ore deposit. Acta Petrologica Sinica 20, 877-886.

Quesnel, B., Boiron, M.-C., Cathelineau, M., Truche, L., Rigaudier, T., Bardoux, G., Agrinier, P., de Saint Blanquat, M., Masini, E. and Gaucher, E.C. (2019) Nature and Origin of Mineralizing Fluids in Hyperextensional Systems: The Case of Cretaceous Mg Metasomatism in the Pyrenees %J Geofluids. 2019, 18.

Rouxhet, P.G., Gillard, J.L. and Fripiat, J.J. (1972) Thermal decomposition of amosite, crocidolite, and biotite. Mineralogical Magazine 38, 583-592.

Saint Blanquat (de), M. (1989) La faille normale ductile du massif du Saint Barthélémy (age et signification de l'extension crustale dans la Zone Nord Pyrénéenne). Université de Montpellier II.

Sanz, J., González-Carreño, T. and Gancedo, R. (1983) On dehydroxylation mechanisms of a biotite in vacuo and in oxygen. Physics and Chemistry of Minerals 9, 14-18.

Sharp, Z.D., Papike, J.J. and Durakiewicz, T. (2003) The effect of thermal decarbonation on stable isotope compositions of carbonates. American Mineralogist 88, 87-92.

Truche, L., Joubert, G., Dargent, M., Martz, P., Cathelineau, M., Rigaudier, T. and Quirt, D. (2018) Clay minerals trap hydrogen in the Earth's crust: Evidence from the Cigar Lake uranium deposit, Athabasca. Earth and Planetary Science Letters 493, 186-197.

Vedder, W. and Wilkins, R. (1969) Dehydroxylation and Rehydroxylation, Oxidation and Reduction of Mica. American Mineralogist 54, 432-509.

Villiéras, F., Tvon, J., Cases, J.M., Zimmermann, J.-L. and Baeza, R. (1992) Dosage et localisation du fer II dans le talc et la chlorite par analyse apectrometrique des gaz de thermolyse. Comptes Rendus de l'Académie des Sciences Paris 315, 1201-1206.

Zhang, M., Hui, Q., Lou, X.-J., Redfern, S.A.T., Salje, E.K.H. and Tarantino, S.C. (2006) Dehydroxylation, proton migration, and structural changes in heated talc: An infrared spectroscopic study. American Mineralogist 91, 816-825.

Ziemiański, P.P., Derkowski, A., Szczurowski, J. and Kozieł, M. (2020) The structural versus textural control on the methane sorption capacity of clay minerals. International Journal of Coal Geology 224, 103483.

Zimmermann, J.-L., Jambon, A. and Guyetand, G. (1988) Manometric and mass spectrometric analysis of fluids in geological materials. GEOCHEMICAL JOURNAL 22, 9-21.